PHOTONICS Research

High-axial-resolution optical stimulation of neurons *in vivo* via two-photon optogenetics with speckle-free beaded-ring patterns

Cheng Jin,[1,†] Chi Liu,[1,†] and Lingjie Kong[1,2,*] (ID)

[1]*State Key Laboratory of Precision Measurement Technology and Instruments, Department of Precision Instrument, Tsinghua University, Beijing 100084, China*
[2]*IDG/McGovern Institute for Brain Research, Tsinghua University, Beijing 100084, China*
Corresponding author: konglj@tsinghua.edu.cn

Two-photon optogenetics has become an indispensable technology in neuroscience, due to its capability in precise and specific manipulation of neural activities. A scanless holographic approach is generally adopted to meet the requirement of stimulating neural ensembles simultaneously. However, the commonly used disk patterns fail in achieving single-neuron resolution, especially in axial dimension, and their inherent speckles decrease stimulation efficiency. Here, we propose a novel speckle-free, beaded-ring pattern for high-axial-resolution optical stimulation of neurons *in vivo*. Using a dye pool and a fluorescent thin film as samples, we verify that, compared to those with disk patterns, higher axial resolution and better localization ability can be achieved with beaded-ring patterns. Furthermore, we perform two-photon based all-optical physiology with neurons in mouse S1 cortex *in vivo*, and demonstrate that the axial resolution obtained by beaded-ring patterns can be improved by 24% when stimulating multiple neurons, compared to that of disk patterns. © 2022 Chinese Laser Press

1. INTRODUCTION

In recent decades, optogenetics has played an increasingly important role in probing functional codes of neurons [1–3]. However, in conventional one-photon stimulation based optogenetics, all neurons in the illumination volume are excited or inhibited, which makes it complex to decipher the neural network. To regulate opsins at single-neuron resolutions specifically, two-photon optogenetics has been demonstrated [4,5].

Considering that opsins are distributed on neural membranes, to perform two-photon optogenetics on specific neural ensembles, there are generally two kinds of stimulation strategies: the spiral scan approach [6,7] and scanless holographic approach [8,9]. The former manipulates neurons by spirally scanning somas with diffraction limited foci. This method requires lower laser energy, but may introduce latency and jitter. The latter approach generates extended patterns to cover whole somas based on computer-generated holography (CGH). This method can stimulate neurons without temporal delay caused by scanning, resulting in a better temporal resolution. However, for commonly used extended patterns, such as disks, the axial resolution deteriorates linearly with the increase in radii [10]. Thus, it is difficult to maintain single-neuron resolution, especially when multiple extended patterns are required to simulate neural ensembles simultaneously [11].

To improve the axial resolution of extended patterns in the scanless holographic approach, temporal focusing (TF) technology is adopted [12]. One TF method uses a spatial light modulator (SLM) to generate an extended pattern through the CGH method, and then uses another SLM to achieve three-dimensional (3D) locations of the pattern [13]. Another TF method, called three-dimensional scanless holographic optogenetics with temporal focusing (3D-SHOT), uses a lens [14] or a diffuser [15] to generate an extended pattern followed by using an SLM to position the pattern in 3D. In both methods, because a grating is introduced in a conjugate plane of the focal plane, two-photon absorption is efficient only at the focal plane where the short pulse width recovers. Thus the axial resolution can be effectively improved. However, the introduction of a grating increases the system complexity and the loss of laser power.

In the scanless holographic approach, speckle usually exists when using CGH for extended pattern generation. As the phase of a light field at the target plane is unconstrained in CGH, there are random energy fluctuations on the generated extended patterns, which are more obvious in two-photon optogenetics [16]. To eliminate speckles, various solutions have been proposed. From the perspective of novel CGH algorithms, holographic speckles can be depressed by introducing an initial phase at target planes [17], using a bandwidth constraint strategy [18,19], adopting zero padding [20], and employing deep

learning [21]. But in these methods, parameters should be optimized for specific goals, which increases computational complexity. From the perspective of hardware development, time averaging of multiple irrelevant holograms can also improve the uniformity of holograms [22,23], but this method is not applicable in two-photon optogenetics as it sacrifices temporal resolution.

Here, we propose a novel scheme to achieve high-axial-resolution optical stimulation of neurons *in vivo* via two-photon optogenetics with the beaded-ring pattern. Different from the TF method, our method can improve axial resolution by just changing the extended holographic pattern from a custom disk shape into a beaded-ring shape. Moreover, as the foci in the beaded-ring pattern are separated from each other, no interference leads to speckles, i.e., our method is speckle free. We compare the intensity distribution and axial resolution of different types of stimulation patterns, and demonstrate that higher spatial resolution can be achieved with our novel patterns. Further, we perform two-photon based all-optical interrogation with neurons in mouse S1 cortex *in vivo*, and demonstrate that the physiological resolution achieved with beaded-ring patterns is better than that with commonly used disk patterns. We expect that the optical stimulation with beaded-ring patterns is a promising strategy for holographic two-photon optogenetics.

2. MATERIALS AND METHODS

A. Optical Setup
We experimentally characterize two-dimensional (2D) intensity distribution of the generated holographic patterns by the vertical detection method [24] with two-photon excited fluorescence in a dye pool of sulforhodamine 101 (CAS#60311-02-6, Shanghai Yuanye Bio-Technology). To test 3D intensity distribution when multiple patterns are generated simultaneously, we build a detection system with opposite-facing objectives (Fig. 1). The device used in the excitation path is equivalent to that of the vertical detection system [24]. The sample is a custom-made thin film of fluorescent paint (Tamiya Color TS-36 Fluorescent Red) on cover glasses. The emission fluorescence is imaged on a CCD (33UX178, DMK) by objective 2 (25×, 1.05 NA, XLPLN25XWMP2, Olympus), a filter (ET750SP-2p8, CHROMA), and a tube lens (TTL200-A, Thorlabs). Fluorescence intensity characterization of 3D volumes is obtained by moving objective 1 (25×, 1.05 NA, XLPLN25XWMP2, Olympus) with a piezo-scanning
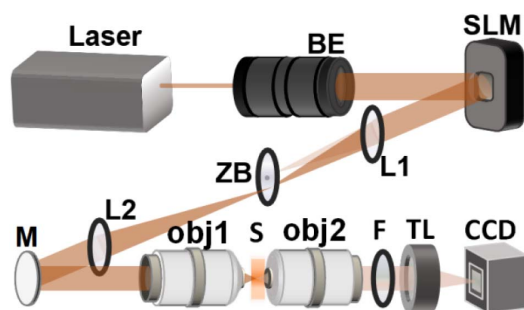
Fig. 1.   Detection system with opposite-facing objectives. BE, beam expander; ZB, zero-order blocker; L, lens; M, mirror; obj, objective; S, sample; F, filter; TL, tube lens.

stage, while objective 2 and the thin film are fixed (the film is at the focal plane of objective 2). To quickly collect hundreds of images in every 3D volume, a data acquisition card (NI PCIe6321, National Instrument) is used to synchronously trigger the piezo-scanning stage and CCD.

To verify the improved performance of our method via two-photon based all-optical physiology *in vivo*, we build a customized two-photon imaging microscope, integrated with a holographic two-photon excitation/inhibition path (similar to the setup in Ref. [6]). An SLM (X10468-07, Hamamatsu) is introduced into the excitation path to display holographic extended patterns [8]. The repetition rate of the femtosecond laser for both imaging ($\lambda = 920$ nm) and stimulation ($\lambda = 1040$ nm) is 80 MHz (Chameleon Discovery, Coherent).

B. System Registration
A hydrogel layer with sulforhodamine 101 is used for the registration between holographic coordinates and imaging coordinates. The weighted Gerchberg-Saxton (GSw) algorithm [25] is used to generate foci of different coordinates at the target imaging plane, and the corresponding phase distribution is loaded onto the SLM. The hydrogel layer is ablated using two-photon stimulation mode with a target phase, and the spatial position of every ablation focus is obtained in two-photon imaging mode. The affine transformation relationship between holographic coordinates and imaging coordinates is calculated with the spatial information of at least three ablation foci. Thus, positions of neurons to be stimulated can be calculated in the SLM coordinate system, and holographic patterns can be generated correspondingly. To improve stimulation accuracy, affine transformation relationships are measured at different depths correspondingly.
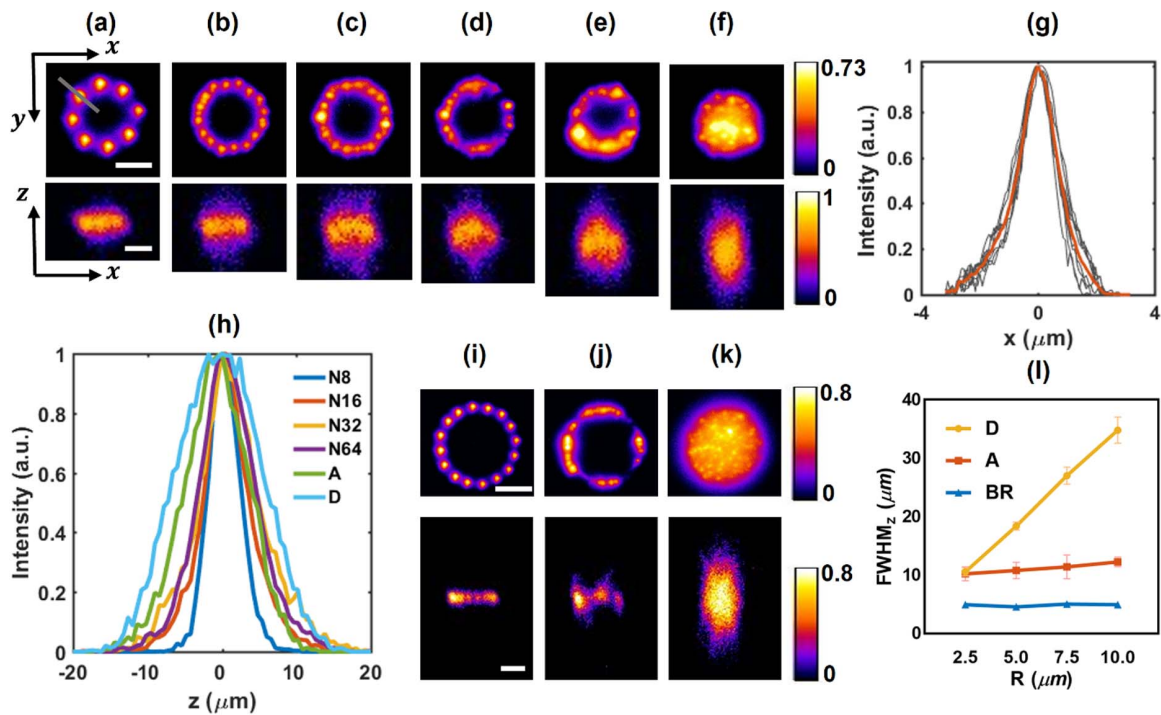
C. Holographic Pattern Generation
Holograms are obtained after 100-times iteration with the GSw algorithm [25]. A disk pattern commonly used for optical simulation covers the whole circle region. In this work, two novel patterns are generated and tested, and compared with the disk pattern. One is an annular pattern, and the other is a beaded-ring pattern, which consists of multiple foci evenly spaced along a circle. For annular patterns, the pattern width is 1 μm, which is defined as outer radius minus inner radius. For beaded-ring patterns, eight foci along a circle with radii of 5 μm are used for most experiments, except the patterns in Figs. 2(b)–2(f). In calculating the holographic phase of beaded-ring patterns, the target size of each bead is one pixel, which corresponds to a transform-limited focus, so that the smallest bead size can be achieved.

In all-optical physiology *in vivo* with two-photon optogenetics experiments, the center of a neuron to be stimulated, which is considered as the center of a target pattern, is manually selected based on the two-photon image at the imaging focal plane with a custom MATLAB program. The center positions of patterns at different depths are calculated based on affine transformation matrices. A series of disk and beaded-ring patterns is generated according to these center positions.

D. Sample Preparation and Anesthesia Operation
All procedures involving mice are approved by the Animal Care and Use Committees of Tsinghua University. We label the

Fig. 2. Characterization of generated holographic patterns for a single target stimulation. (a)–(f) Two-photon intensity distributions in xy (upper) and xz (lower) section of beaded ring of 8, 16, 32, and 64 foci, annular, and disk patterns with 5 μm radius, respectively. Scale bar: 5 μm. (g) Lateral intensity distribution of each focus in (a) and the average lateral intensity of all eight foci, labeled with gray and red lines, respectively. (h) Axial intensity distribution of different patterns shown in (a)–(f). N8, beaded-ring pattern of eight foci (N16, N32, and N64 have similar definitions); A, annular pattern; D, disk pattern. (i)–(k) Two-photon intensity distributions in xy (upper) and xz (lower) section of beaded-ring of 16 foci, annular, and disk patterns with 10 μm radius, respectively. Scale bar: 10 μm. (l) Axial resolution of the beaded-ring, annular, and disk patterns with different radii. D, disk pattern; A, annular pattern, BR, beaded-ring pattern. Five patterns of different radii for each type are generated, and the center of each pattern is 20 μm away from the origin. The data shown in (l) are the mean and standard deviation of axial resolutions of five patterns.

neurons in mouse L2/3 of S1 cortex via virus infection with a single integrated ChRmine/GCaMP6m virus [26]. Around 300 nL virus is injected at 250 μm depth from the surface of S1 cortex, in 7–8 min. After two weeks of virus expression, chronic optical windows are installed after craniotomy [27]. Then after one week's recovery, all-optical physiology tests are performed with the mice being anesthetized with isoflurane, using a small animal gas anesthesia machine (R520IP, RWD Life Science).

E. Data Processing

In fluorescence intensity characterization experiments, we integrate intensity within the target pattern at each z depth to obtain the axial intensity distribution curve. The full width at half maximum (FWHM) of the axial intensity distribution curve is defined as the axial resolution of a pattern, whether for a 2D or 3D one. The peak value of an axial intensity curve is defined as the maximum intensity, which is used to characterize the energy of a pattern.

To process data in all-optical physiology experiments, a customized MATLAB code is used. After summing two-photon signals in a target neuron region and removing background near the neuron, the calcium signal response F in each frame is obtained. The change of calcium signal δF arising from two-photon optogenetics is defined as the maximum calcium signal caused by stimulation minus the calcium signal just one frame

before stimulation. The neural activity response curve is obtained by Gaussian fitting of δF at different depths, and its FWHM is defined as the physiological resolution of this neuron [6,14].

3. RESULTS

A. 2D Performance Characterization of Holographic Patterns

We first use a vertical detection system for the characterization of a single holographic pattern. For a beaded-ring pattern, when eight foci equally spaced along the circle with radii of 5 μm are generated, the average lateral resolution of these foci is 1.5 μm [Figs. 2(a) and 2(g)], while the axial resolution is 4.56 ± 0.33 μm (mean ± standard deviation). For patterns with the same radius, the axial resolution of an annular pattern is worse (10.8 ± 1.41 μm), and that of a disk pattern is the worst (18.36 ± 0.68 μm). As shown in Figs. 2(a)–2(f) and 2(h), with the increase in focal numbers, the axial resolution gradually deteriorates until it is similar to that of an annular pattern. For disk patterns of different radii, the axial resolution increases linearly with the increase in radius. In contrast, the axial resolution has no significant change with the change of radius for both annular and beaded-ring patterns, and the axial resolution of beaded-ring patterns is always better [Fig. 2(l)].

Next, we characterize multiple holographic patterns with the vertical detection system. The intensity distributions of multiple patterns generated on the same lateral and axial plane by different schemes are shown in Figs. 3(a)–3(c) and Figs. 3(d)–3(f). As shown in Figs. 3(g) and 3(h), higher axial resolution can be achieved with beaded-ring patterns, for both lateral and axial multiple pattern generation. Especially, when multiple targets are generated on different axial planes, part of the energy is distributed in non-targeted areas for disk patterns [Fig. 3(f)] and annular patterns [Fig. 3(e)]. Significantly, this phenomenon can be avoided in the case of beaded-ring patterns [Fig. 3(d)].

## B. 3D Performance Characterization of Holographic Patterns

We further characterize multiple holographic patterns in 3D [Figs. 4(a)–4(c)], using a detection system with opposite-facing objectives, shown in Fig. 1. The GSw algorithm is used to generate 10 targets of beaded-ring, annular, and disk patterns. They all have radii of 5 µm and are distributed in a 3D space of 100 µm × 100 µm × 150 µm. For beaded-ring patterns, there is almost no energy distribution in non-target areas [Fig. 4(a)]. However, for disk patterns, the energy distribution in non-target areas is high [Fig. 4(c)], which may lead to off-target stimulation in two-photon optogenetics. The axial resolution of beaded-ring patterns is more than twice better, compared to that of annular and disk patterns [Fig. 4(d)]. In addition, under the same excitation power level, the average

signal intensity and signal uniformity of generated beaded-ring patterns are the highest among these three types of patterns [Fig. 4(e)]. All the above demonstrate that the beaded-ring pattern has the best capability in spatial confinement and is the most favorable for two-photon optogenetics.

C. All-Optical Physiology *in vivo* with Two-Photon Optogenetics

To verify the performance enhancement of our proposed beaded-ring patterns for two-photon optogenetics *in vivo*, we perform experiments based on an all-optical physiology system. Specific holograms are loaded on the SLM to stimulate target neurons with different types of patterns, and the corresponding responses of neurons are recorded by two-photon fluorescence imaging of the calcium indicator GCaMP6 [Fig. 5(a)]. By imaging 1 µm fluorescent beads with generated holographic patterns in the stimulation path, the convolutions of illumination patterns with fluorescent beads are obtained as shown in the lower right of Fig. 5(a), which demonstrates the typical intensity distribution of disk and beaded-ring patterns in our all-optical physiology system under the same excitation power. In the scenario of a disk pattern, significant speckles show up, which would definitely lead to low stimulation efficiency. In contrast, a beaded-ring pattern whose foci are evenly distributed on a circle does not interfere with the speckles.

We achieve the location of neurons with two-photon imaging mode. For a target neuron in an imaging field of view [Fig. 5(b)], two-photon optogenetics based on disk and
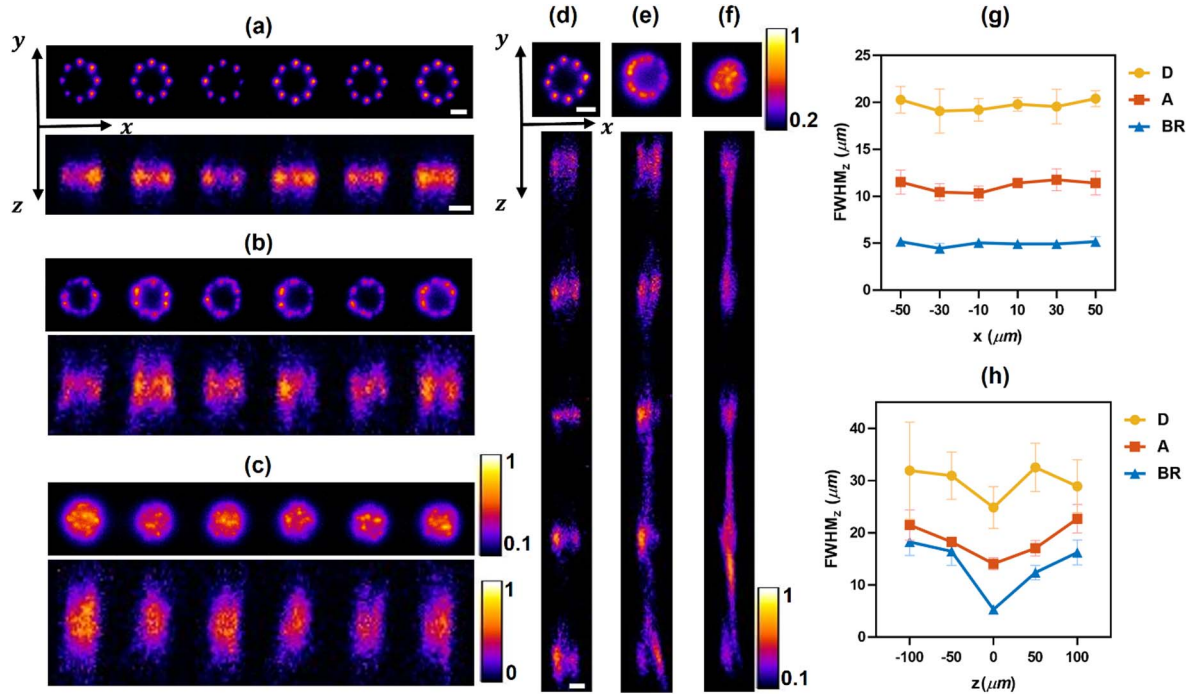

Fig. 3. Characterization of generated holographic patterns for multiple target stimulation in a plane. (a)–(f) Two-photon intensity distributions in *xy* (upper) and *xz* (lower) section of beaded-ring, annular, and disk patterns, respectively. (a)–(c) Targets are in the same lateral section (*xy*), whose centers are from −50 to 50 µm with a lateral interval of 20 µm. (d)–(f) Targets are in the same axial section (*xz*), whose centers are from −100 to 100 µm with an axial interval of 50 µm. (g), (h) Axial resolution of every pattern in (a)–(c) and (d)–(f), respectively. Scale bar: 5 µm. All pattern distributions in (a)–(f) are obtained under the same excitation power level. D, disk pattern; A, annular pattern; BR, beaded-ring pattern. Five groups of patterns in different distributions (*xy* or *xz*) of each type are generated, and the distances from patterns of different groups to the center of the field of view are equal for the same distribution. The data shown in (g), (h) are the mean and standard deviation of axial resolutions of five group patterns.
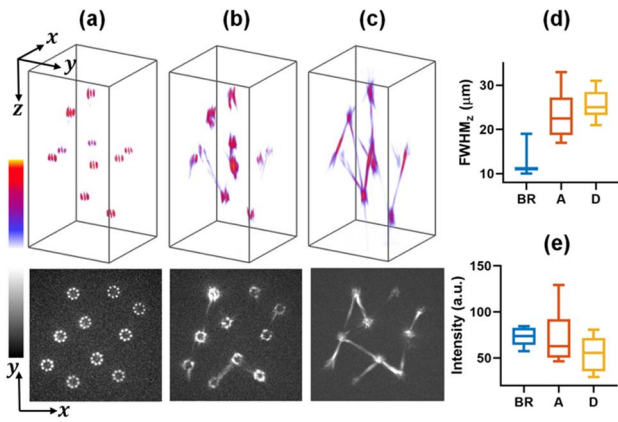
Fig. 4. Characterization of generated holographic patterns for multiple target stimulation in 3D stack. (a)–(c) Intensity distributions (upper) and maximum intensity projections in *xy* section (lower) of 10 targets with beaded-ring, annular, and disk patterns, respectively. Radius of each pattern: 5 μm. Stack size: 120 μm × 120 μm × 240 μm. (d) Statistical analysis of axial resolutions of each pattern in (a)–(c). (e) Statistical analysis of maximal intensities of each pattern in (a)–(c). The central mark of each box in (d), (e) indicates the median, while the bottom and top edges of the boxes indicate the 25th and 75th percentiles, respectively. BR, beaded-ring pattern; A, annular pattern; D, disk pattern.

beaded-ring patterns is employed to stimulate the neuron, and duration is 100 ms for each stimulation. Here, a long duration is chosen to improve responses of neurons and avoid the signal drowning in noise, as it decreases when stimulation patterns move away from neurons along *z* axis. To restore opsin after each stimulation, we set a dark interval of at least 60 s between two tests. To avoid pseudo activation of neurons by the imaging beam, the imaging power is reduced as much as possible so that the calcium baseline of neurons can hardly be seen when only two-photon imaging is performed. The powers of stimulation and imaging vary slightly due to different expression levels of opsins and calcium indicators among different neurons in different mice.

The stimulation depth where the maximum δF is obtained among a series of stimulation depths is defined as the optimal stimulation depth. We find that a target neuron can be stimulated by both types of patterns at their optimal stimulation depths with the same excitation power [Fig. 5(c)]. δF decreases gradually when deviating from the optimal stimulation depth, and the decrease rate is faster for the case with a beaded-ring pattern than that with a disk pattern [Fig. 5(d)]. By testing and analyzing physiological resolutions [6,14] of 10 neurons with single-neuron stimulations, we find that the axial resolution under optical stimulation with beaded-ring patterns (25.91 ± 7.57 μm) is significantly better than with disk patterns (40.68 ± 8.33 μm), as shown in Fig. 5(e). The improvement is as much as 36.3%, which indicates the capability of
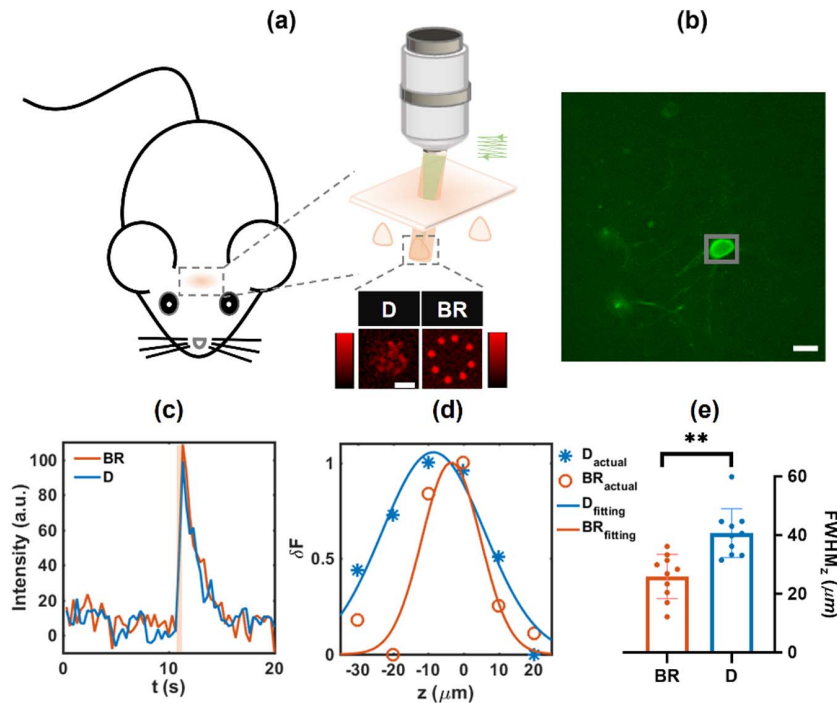
Fig. 5. All-optical physiology test with different stimulation patterns on a single neuron *in vivo*. (a) Schematic diagram of the all-optical physiology system. Green: beam for two-photon calcium imaging. Red: beam for two-photon optogenetics. Diagram at lower right: excitation pattern distribution tested by the all-optical physiology system with 1 μm fluorescent beads. D, disk pattern; BR, beaded-ring pattern. Scale bar: 5 μm. (b) Two-photon image of a neuron in L2/3 of mouse S1 cortex, infected with a ChRmine/GCaMP6m virus. Scale bar: 10 μm. (c) Calcium signal of a neuron under different stimulation patterns at the optimal stimulation depth. (d) Changes in calcium signal caused by two-photon optogenetics at different stimulation depths under different stimulation patterns. The fitted response intensity curves are shown with solid lines. (e) Statistical analysis of axial resolutions under different stimulation schemes. Data are from 10 neurons in three mice. $**\, p = 0.0017$, ratio paired *t* test.

(a)
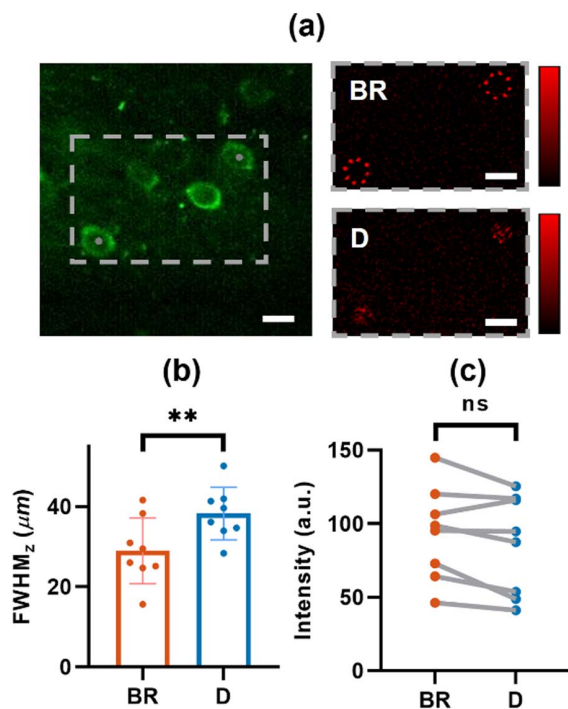
Fig. 6. All-optical physiology test with different stimulation patterns on multiple neurons simultaneously *in vivo*. (a) Left: typical two-photon image of neurons in L2/3 of mouse S1 cortex, infected with a ChRmine/GCaMP6m virus. Locations of gray spots are the center of two excitation patterns. Right: distribution of excitation patterns to stimulate target neurons. D, disk pattern; BR, beaded-ring pattern. Scale bar: 10 μm. (b) Mean axial resolutions of calcium signals of multiple neurons under different stimulation schemes. Data are from eight groups, and each group has two neurons to be stimulated. $** p = 0.0086$, ratio paired t test. (c) Mean peak responses of multiple neurons at their optimal stimulation depths under different stimulation schemes. Data are from eight groups, and each group has two neurons to be stimulated. ns, not significant; $p = 0.0638$, ratio paired t test.
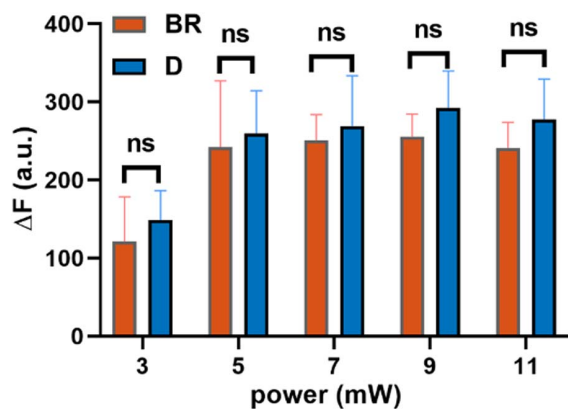
Fig. 7. Calcium signal of neurons with different types of stimulation patterns, at different stimulation powers. BR, beaded-ring pattern; D, disk pattern; ns, not significant. $p = 0.30, 0.35, 0.43, 0.12$, and 0.36 for stimulation power with 3, 5, 7, 9, and 11 mW, respectively, ratio paired t test. Duration of each stimulation: 100 ms. Data are from three neurons, and each neuron is stimulated with two stimulation patterns at different stimulation powers.

optical stimulation by beaded-ring patterns at single-neuron resolutions.

Next, we perform two-photon optogenetics stimulation and two-photon calcium signal imaging experiments on multiple neurons simultaneously. As shown in Fig. 6(a) left, two neurons to be stimulated are selected in the same field of view, limited by the available laser power. Then, beaded-ring and disk patterns matching these two neurons are used for stimulation [Fig. 6(a) right], with duration of 100 ms. Two neurons stimulated at the same time are defined as a group. Compared with disk patterns, the average axial resolution of neurons in a group stimulated by beaded-ring patterns is increased by 24.27% [Fig. 6(b)], from 38.24 ± 6.55 μm to 28.96 ± 8.19 μm. The mean peak responses of beaded-ring patterns are not significantly different from that of disk patterns [Fig. 6(c)], which shows that the beaded-ring pattern has comparable excitation efficiency with the disk pattern at the optimal stimulation depth.

4. DISCUSSION AND CONCLUSION

Considering that opsins are distributed on the cellular membrane, using a beaded-ring pattern focused on the membrane allows the photostimulation of opsins more efficiently. However, the responses of neurons depend not only on the photostimulation intensity on opsins, but also on the overall illumination volumes of opsins. We test the responses of neurons with stimulations of beaded-ring and disk patterns at different powers (Fig. 7). With the increase in stimulation power, neural responses tend to be saturated under both stimulation patterns. There is no significant difference in neural responses induced by beaded-ring and disk patterns at the same stimulation power.

In this paper, we propose a novel speckle-free, beaded-ring pattern for holographic two-photon optogenetics *in vivo*. Compared with conventional disk patterns, higher axial resolution can be achieved with beaded-ring patterns. Also, the axial resolution of a beaded-ring pattern is not affected by the increase in radius. When multiple patterns are generated simultaneously in 3D space, the laser power of beaded-ring patterns can be restricted in target regions, while laser power often flows to non-target regions when disk patterns are generated. Through all-optical physiology tests *in vivo*, we demonstrate that the physiological resolution in axial dimension can be improved by as much as 24.27% by using beaded-ring patterns compared to that with disk patterns. We expect a broad application of our proposed beaded-ring patterns for holographic two-photon optogenetics.

Disclosures. The authors declare no conflicts of interest.

Data Availability. All data presented in this paper are available upon reasonable request from the corresponding author.

†These authors contributed equally to this paper.

REFERENCES

1. E. S. Boyden, F. Zhang, E. Bamberg, G. Nagel, and K. Deisseroth, "Millisecond-timescale, genetically targeted optical control of neural activity," Nat. Neurosci. **8**, 1263–1268 (2005).
2. V. Szabo, C. Ventalon, V. De Sars, J. Bradley, and V. Emiliani, "Spatially selective holographic photoactivation and functional fluorescence imaging in freely behaving mice with a fiberscope," Neuron **84**, 1157–1169 (2014).
3. K. Daie, K. Svoboda, and S. Druckmann, "Targeted photostimulation uncovers circuit motifs supporting short-term memory," Nat. Neurosci. **24**, 259–265 (2021).
4. V. Nikolenko, K. E. Poskanzer, and R. Yuste, "Two-photon photostimulation and imaging of neural circuits," Nat. Methods **4**, 943–950 (2007).
5. H. Adesnik and L. Abdeladim, "Probing neural codes with two-photon holographic optogenetics," Nat. Neurosci. **24**, 1356–1366 (2021).
6. W. Yang, L. Carrillo-Reid, Y. Bando, D. S. Peterka, and R. Yuste, "Simultaneous two-photon imaging and two-photon optogenetics of cortical circuits in three dimensions," eLife **7**, e32671 (2018).
7. R. Prakash, O. Yizhar, B. Grewe, C. Ramakrishnan, N. Wang, I. Goshen, A. M. Packer, D. S. Peterka, R. Yuste, M. J. Schnitzer, and K. Deisseroth, "Two-photon optogenetic toolbox for fast inhibition, excitation and bistable modulation," Nat. Methods **9**, 1171–1179 (2012).
8. A. Forli, D. Vecchia, N. Binini, F. Succol, S. Bovetti, C. Moretti, F. Nespoli, M. Mahn, C. A. Baker, M. M. Bolton, and O. Yizhar, "Two-photon bidirectional control and imaging of neuronal excitability with high spatial resolution *in vivo*," Cell Rep. **22**, 3087–3098 (2018).
9. J. V. Gill, G. M. Lerman, H. Zhao, B. J. Stetler, D. Rinberg, and S. Shoham, "Precise holographic manipulation of olfactory circuits reveals coding features determining perceptual detection," Neuron **108**, 382–393 (2020).
10. C. Lutz, T. S. Otis, V. DeSars, S. Charpak, D. A. DiGregorio, and V. Emiliani, "Holographic photolysis of caged neurotransmitters," Nat. Methods **5**, 821–827 (2008).
11. E. Papagiakoumou, E. Ronzitti, I. W. Chen, M. Gajowa, A. Picot, and V. Emiliani, "Two-photon optogenetics by computer-generated holography," in *Optogenetics: A Roadmap* (Springer, 2018), pp. 175–197.
12. E. Papagiakoumou, V. De Sars, D. Oron, and V. Emiliani, "Patterned two-photon illumination by spatiotemporal shaping of ultrashort pulses," Opt. Express **16**, 22039–22047 (2008).
13. O. Hernandez, E. Papagiakoumou, D. Tanese, K. Fidelin, C. Wyart, and V. Emiliani, "Three-dimensional spatiotemporal focusing of holographic patterns," Nat. Commun. **7**, 11928 (2016).
14. N. C. Pégard, A. R. Mardinly, I. A. Oldenburg, S. Sridharan, L. Waller, and H. Adesnik, "Three-dimensional scanless holographic optogenetics with temporal focusing (3D-SHOT)," Nat. Commun. **8**, 1 (2017).
15. G. J. Goldey, D. K. Roumis, L. L. Glickfeld, A. M. Kerlin, R. C. Reid, V. Bonin, D. P. Schafer, and M. L. Andermann, "Removable cranial windows for long-term imaging in awake mice," Nat. Protoc. **9**, 2515–2538 (2014).
16. E. Ronzitti, C. Ventalon, M. Canepari, B. C. Forget, E. Papagiakoumou, and V. Emiliani, "Recent advances in patterned photostimulation for optogenetics," J. Opt. **19**, 113001 (2017).
17. H. Pang, J. Wang, A. Cao, and Q. Deng, "High-accuracy method for holographic image projection with suppressed speckle noise," Opt. Express **24**, 22766–22776 (2016).
18. L. Chen, S. Tian, H. Zhang, L. Cao, and G. Jin, "Phase hologram optimization with bandwidth constraint strategy for speckle-free optical reconstruction," Opt. Express **29**, 11645–11663 (2021).
19. X. Sui, Z. He, G. Jin, D. Chu, and L. Cao, "Band-limited double-phase method for enhancing image sharpness in complex modulated computer-generated holograms," Opt. Express **29**, 2597–2612 (2021).
20. W. Qu, H. Gu, and Q. Tan, "Holographic projection with higher image quality," Opt. Express **24**, 19179–19184 (2016).
21. D. Y. Park and J. H. Park, "Hologram conversion for speckle free reconstruction using light field extraction and deep learning," Opt. Express **28**, 5393–5409 (2020).
22. J. Amako, H. Miura, and T. Sonehara, "Speckle-noise reduction on kinoform reconstruction using a phase-only spatial light modulator," Appl. Opt. **34**, 3165–3171 (1995).
23. L. Golan and S. Shoham, "Speckle elimination using shift averaging in high-rate holographic projection," Opt. Express **17**, 1330–1339 (2009).
24. C. Jin, C. Liu, R. Shi, and L. Kong, "Precise 3D computer-generated holography based on non-convex optimization with spherical aberration compensation (SAC-NOVO) for two-photon optogenetics," Opt. Express **29**, 20795–20807 (2021).
25. R. Di Leonardo, F. Ianni, and G. Ruocco, "Computer generation of optimal holograms for optical trap arrays," Opt. Express **15**, 1913–1922 (2007).
26. J. H. Marshel, Y. S. Kim, T. A. Machado, S. Quirin, B. Benson, J. Kadmon, C. Raja, A. Chibukhchyan, C. Ramakrishnan, M. Inoue, and J. C. Shane, "Cortical layer–specific critical dynamics triggering perception," Science **365**, eaaw5202 (2019).
27. A. R. Mardinly, I. A. Oldenburg, N. C. Pégard, S. Sridharan, E. H. Lyall, K. Chesnov, S. G. Brohawn, L. Waller, and H. Adesnik, "Precise multimodal optical control of neural ensemble activity," Nat. Neurosci. **21**, 881–893 (2018).